computers. Mrs S. Foster is kindly thanked for typing the manuscript.

References

ALEXANDER, L. E. & SMITH, G. S. (1964). *Acta Cryst.* **17**, 1195–1201.

ALLMANN, R. (1968). *Z. Kristallogr.* **126**, 417–426.

AMINOFF, G. (1921). *Z. Kristallogr.* **56**, 506–509.

BAUER, L. H. & BERMAN, H. (1929). *Am. Mineral.* **14**, 165–172.

BAUR, W. H. (1970). *Trans. Am. Crystallogr. Assoc.* **6**, 129–155.

BAUR, W. H. (1972). *Am. Mineral.* **57**, 709–731.

BROWN, I. D. & WU, K. K. (1976). *Acta Cryst.* B**32**, 1957–1959.

COPPENS, P. (1974). *Acta Cryst.* B**30**, 255–261.

FERRARIS, G. & FRANCHINI-ANGELA, M. (1972). *Acta Cryst.* B**28**, 3572–3583.

FINNEY, J. J. (1969). *Am. Mineral.* **54**, 973–975.

GHOSE, S. (1964). *Acta Cryst.* **17**, 1051–1057.

HILL, R. J. (1979). *Aust. Mineral.* No. 26, pp. 126–128.

HILL, R. J., GIBBS, G. V. & PETERSON, R. C. (1979). *Aust. J. Chem.* **32**, 231–241.

HORNSTRA, J. & STUBBE, B. (1972). PW 1100 data-processing program. Philips Research Laboratories, Eindhoven, Holland.

International Tables for X-ray Crystallography (1974). Vol. IV. Birmingham: Kynoch Press.

LARSON, A. C. (1967). *Acta Cryst.* **23**, 664–665.

LOUISNATHAN, S. J., HILL, R. J. & GIBBS, G. V. (1977). *Phys. Chem. Miner.* **1**, 53–69.

MCLARNAN, T. J., HILL, R. J. & GIBBS, G. V. (1979). *Aust. J. Chem.* **32**, 949–959.

PAULING, L. (1960). *The Nature of the Chemical Bond*, 3rd ed. Ithaca: Cornell Univ. Press.

PETERSON, R. C., HILL, R. J. & GIBBS, G. V. (1978). *Geol. Soc. Am. Abstr. Program*, **10**, 471.

PREWITT-HOPKINS, J. (1949). *Am. Mineral.* **34**, 589–595.

SHANNON, R. D. (1976). *Acta Cryst.* A**32**, 751–767.

SHELDRICK, G. M. (1976). *SHELX* 76. Program for crystal structure determination. Univ. of Cambridge, England.

STAHLIN, W. & OSWALD, H. R. (1970). *Acta Cryst.* B**26**, 860–863.

STEWART, J. M. (1976). Editor. The XRAY system – version of 1976. Tech. Rep. TR-446. Computer Science Center, Univ. of Maryland, College Park, Maryland.

STEWART, R. F., DAVIDSON, E. R. & SIMPSON, W. T. (1965). *J. Chem. Phys.* **42**, 3175–3187.

TOSSELL, J. A. & GIBBS, G. V. (1976). *J. Mol. Struct.* **35**, 273–287.

ZIGAN, F. & ROTHBAUER, R. (1967). *Neues Jahrb Mineral. Monatsh.* pp. 137–143.

Acta Cryst. (1980). B**36**, 1311–1319

The Nature of the Chemical Bonding in Boron Carbide, $B_{13}C_2$. III. Static Deformation Densities and Pictorial Representation

BY A. KIRFEL, A. GUPTA AND G. WILL

Mineralogisches Institut der Universität Bonn, Lehrstuhl für Mineralogie und Kristallographie, Poppelsdorfer Schloss, 5300 Bonn, Federal Republic of Germany

(*Received* 1 *December* 1979; *accepted* 8 *January* 1980)

Abstract

The crystal structure of rhombohedral $B_{13}C_2$ is composed of two structural units, the linear C—B—C chain and the B_{12} icosahedron distorted from ideal symmetry due to the different external bonding partners. Based on multipole expansion results, static deformation density maps have been calculated for sections of interest in both units. These static deformation density distributions are discussed in comparison to earlier published dynamic deformation density results. Three-dimensional pictorial representations of the static deformation densities and of total static densities of individual atoms as well as of structural fragments are given to complete the information obtainable from a multipole expansion refinement and to give a better insight into the chemical bonding in $B_{13}C_2$.

0567-7408/80/061311-09$01.00

Introduction

In two previous papers (Kirfel, Gupta & Will, 1979*a*,*b*), hereafter called I and II, the crystal structure of $B_{13}C_2$ has been studied in detail by least-squares refinements of X-ray diffraction data (I). These studies included a multipole expansion refinement (Hirshfeld, 1971; Harel & Hirshfeld, 1975), which yielded $R = 0{\cdot}028$ compared to $R = 0{\cdot}050$ for the conventional spherical-atom refinement. The numerical results like

atomic positional and vibrational parameters, bond distances and angles and rigid-bond tests (Hirshfeld, 1976) have been presented in I.

Subsequent calculations of the dynamic deformation density and valence density distributions in selected sections of interest of the two structural units constituting $B_{13}C_2 = (CBC)B_{12}$, namely the linear C–B–C chain and the B_{12} icosahedron (Fig. 1), revealed significant charge accumulations between the atoms as a result of the covalent bonding (II). These investigations led to the observation of a strong interaction within the C–B–C chain composed of covalent bonding and Coulomb forces resulting from a charge transfer from the central B atom towards the C atoms. For the icosahedron we found charge distributions which we interpreted in terms of distorted three-center interactions and simultaneously by a classical covalent bonding model. Between adjacent icosahedra there are strong B–B bonds, and the bonding between the icosahedra and the C–B–C chains is provided by the existence of puckered graphite-like layers of B_4C_2 hexagons running perpendicular to the C–B–C chains (Will, Kirfel & Gupta, 1979). In addition, for the first time experimental evidence was presented for a charge transfer of about one electron from the chain towards the icosahedron as demanded by Longuet-Higgins & Roberts (1955) to stabilize the icosahedron. Consequently, we found the total distribution of bonds rather isotropic, which explains the great stability of boron carbide (m.p. of B_4C = 2623 K, hardness 9·5) and of similar compounds (like elementary β-rhombohedral boron).

The ensuing work on this compound was devoted to making use of the refined localized linear combinations of the atomic deformation functions from the multipole refinement, which are considered to represent the static deformation density distribution of the atomic electron shells. Since this distribution,

$$d\rho(\mathbf{r}) = \sum_j \sum_l c_{jl}\, \psi_{jl},$$

is in analytical form, which can be handled easily, conventional two-dimensional representations of selected sections can be obtained without difficulties. The same applies for the associated distributions of e.s.d.'s, which can be calculated from the e.s.d.'s of the multipole coefficients and the correlation matrix. In this part we present and discuss the static deformation densities in comparison to the results of dynamic deformation densities of II. In addition, we have also calculated and plotted three-dimensional representations at constant electron density levels of the static deformation density of individual atoms as well as of molecular fragments. These give a vivid impression of the deviations of the electron distribution in the crystal from that of the conventionally used free spherical-atom model.

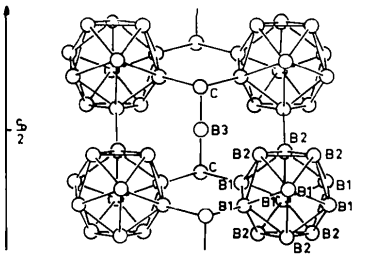

Fig. 1. Structure of $B_{13}C_2$ showing the linear C–B–C chain and the B_{12} icosahedra.

Static deformation densities

Since the crystal structure so far has been treated as being built up of two distinguishable structural elements, the C–B–C chain and the B_{12} icosahedron, the presentation and discussion of the static deformation densities is divided into (i) bonding within the two molecular fragments; (ii) bonding between the fragments.

(*a*) *The* C–B–C *chain*

Fig. 2 depicts the linear static deformation density along the short B(3)–C bond (1·429 Å) lying on the crystallographic *c* axis. The dotted line shows the e.s.d. $\sigma(d\rho_{stat})$. The relatively large uncertainties of at most 0·7 e Å^{-3} at the atomic positions compare well with the corresponding peak heights of the e.s.d. of the dynamic deformation density (II) having been calculated according to the method outlined by Rees (1976, 1978). As for $d\rho_{dyn}$, the static deformation density distribution shows a trough at the B atom site, which indicates a charge transfer within the chain towards the C atoms. This trough is followed by a pile-up of bond density between the atoms with a flat maximum of 1·0 e Å^{-3}. Such a charge accumulation can only result from a strong covalent bond overlap, and necessarily renders the conventional spherical-atom model inadequate for an accurate description of the electron distribution in the chain. The linear deformation density shows at the C atom site, in contrast to the results of $d\rho_{dyn}$ (II), a distribution affected by a strong dipole contribution. The polarization of the bonded C atom towards the central B(3) leads to an asymmetric shape of the initially symmetric electron shell of the free atom. Since in conventional refinement procedures, a symmetric (Gaussian) function is always fitted to such an asymmetric distribution, a too short B(3)–C distance will be observed. In fact, the B(3)–C distances calculated from the different refinements of I show in comparison to the conventional all-data refinement

[1·429 (1) Å] a slight elongation for the high-order refinements (0·002 Å) and a significant one (0·009 Å) for the multipole refinement. This example may demonstrate that the evaluation of the fine structure of the electron density can require improved electron density models, which allow analytical descriptions of asymmetric charge distributions. It also shows that the high-order refinement technique by itself cannot generally prevent parameter bias in the case of polarized atoms, since the asymmetry of the electron shell may still be significant close to the atomic center and this will also affect high-order scattering.

A two-dimensional representation of the static deformation density associated with the C—B—C chain is given in Fig. 3(*a*). Fig. 3(*b*) shows the corresponding distribution of the e.s.d. $\sigma(\mathrm{d}\rho_{\mathrm{stat}})$. The plane of Fig. 3 is a crystallographic mirror plane containing the *c* axis and the four atoms of the asymmetric unit: B(1), B(2), B(3) and C. The white areas around the atomic positions correspond, in this and all similar maps, to the regions where $\sigma(\mathrm{d}\rho_{\mathrm{stat}}) > 0{\cdot}1$ e Å^{-3}. As in Fig. 2, we can clearly see the charge transfer in the chain, the strong covalent bonding between B(3) and C, and the polarization of the C atom. Apart from this polarization the plot of $\mathrm{d}\rho_{\mathrm{stat}}$ (Fig. 3*a*) fully corroborates the results of the dynamic deformation density and the valence density distribution (II), from which we conclude that the bonding in the chain is composed of B(*sp*) and C(sp^3) hybrid-orbital overlap and Coulomb attraction of the differently charged atoms.

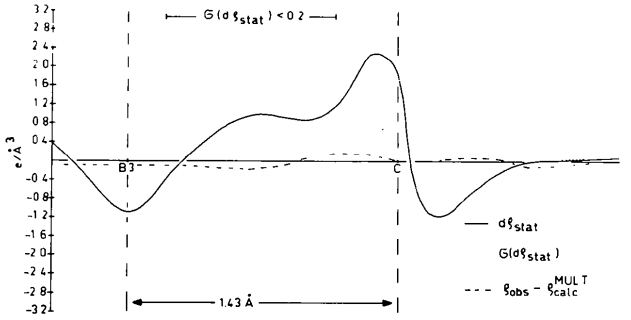

Fig. 2. Linear distribution of the static deformation density $\mathrm{d}\rho_{\mathrm{stat}}$, e.s.d. $\sigma(\mathrm{d}\rho_{\mathrm{stat}})$, and the final residual density $\Delta\rho$ along B(3)—C.

The large amount of electron density between B(3) and C represented by the static deformation density casts doubt on the validity of this finding. An answer can be found from the calculation of a residual density synthesis using the final multipole expansion refinement $F_{\mathrm{h}}^{\mathrm{calc}}$ for the density ρ_{calc}. The broken line in Fig. 2 shows this residual density along B(3)—C. All along and beyond this bond $\Delta\rho < 1{\cdot}5\sigma(\mathrm{d}\rho_{\mathrm{stat}})$. Fig. 3(*c*) depicts the final $\Delta\rho$ in the plane of Fig. 3(*a*). (Note here the peak in the large cavity on the *c* axis, which has been discussed already in II. Obviously, the multipole expansion model did not deal with this charge accumulation.)

Including the observation of equally insignificant residual density values along the C—B(1) bond, we can so far conclude that the refined multipole expansion describes the electron distribution in the C—B—C moiety and its external bonds well. Consequently, we can assign physical relevance to the static deformation density distribution evaluated for this part of the structure.

(*b*) *The* B_{12} *icosahedron*

The B_{12} icosahedron is distorted from its ideal symmetry by the different external bonding partners. The surface consists of twenty triangles, of which three are unique. A detailed description of these triangles (bond lengths and angles) has been given in I and II. Here we present the static deformation densities in the triangle planes and hence the indicated bonding features on the surface of the icosahedron.

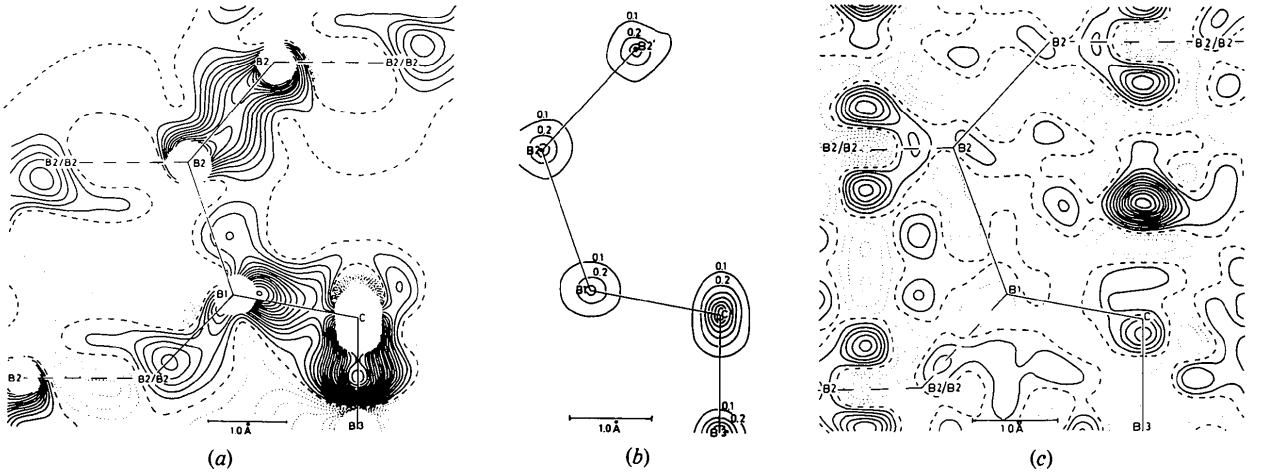

(*a*) (*b*) (*c*)

Fig. 3. (*a*) Static deformation density distribution in the B(3), C, B(1), B(2) plane. Levels at 0·05 e Å^{-3}, negative contours dotted. (*b*) E.s.d. of $\mathrm{d}\rho_{\mathrm{stat}}$ of (*a*). (*c*) Final residual density $\Delta\rho = (1/K)\rho_{\mathrm{obs}} - \rho_{\mathrm{calc}}^{\mathrm{mult}}$. Levels at 0·05 e Å^{-3}, negative contours dotted.

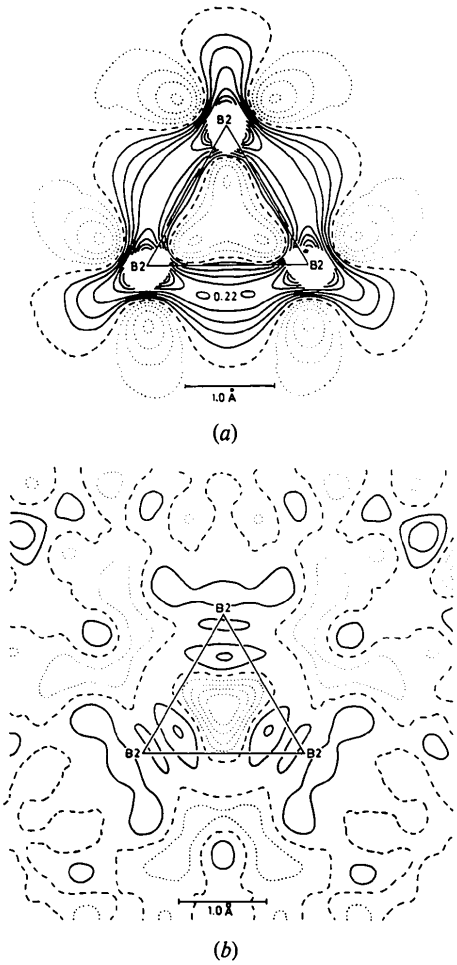

(*a*)

(*b*)

Fig. 4. (*a*) Static deformation density distribution in the plane B(2)–B(2)–B(2) (triangle I). Levels at 0·05 e Å^{-3}, negative contours dotted. (*b*) Final residual density $\Delta\rho$. Levels at 0·05 e Å^{-3}, negative contours dotted.

Triangle (I), B(2)–B(2)–B(2) (Fig. 4*a*), is equilateral with the threefold *c* axis running through the center. In agreement with the results of the dynamic deformation density study of II, the multipole expansion shows well-developed bent bonds between B(2) and B(2). They are represented by almost uniform density bands of at most 0·22 e Å^{-3}. This value compares well with the external dynamic deformation density peak of 0·17 e Å^{-3} (II). However, the charge accumulation in the center of the triangle (0·19 e Å^{-3}; II), which can be considered as an essential feature of a three-center interaction density distribution, is not reproduced in $d\rho_{stat}$. This is a serious disagreement. In case the central charge accumulation could not be described by the multipole expansion model, it should still be present in the final residual density (Fig. 4*b* and Fig. 3*c*). However, even there we find a negative region in the triangle center accompanied by two significant peaks of 0·25 e Å^{-3} above and below the plane (Fig. 3*c*). An explanation for these deviations of ρ_{calc} from ρ_{obs} can be found by considering the special positional character of the trough and peak positions and remembering that the observed F_{00l} are the Fourier coefficients of the unit-cell density projected on the *c* axis. Then, due to the space-group symmetry, the density at the center of triangle (I) ($z = 0{\cdot}5533$) lies between B(3) ($z = 0{\cdot}5$) and C ($z = 0{\cdot}6175$) with about five times the bond density between the chain atoms. This outstanding density distribution will therefore not only determine the adjustment of the B(3) and C multipole functions but also to some extent that of the B(2) functions. This may lead to F_{00l}^{calc} values which produce a total ρ_{calc} along *c* fitting ρ_{obs} within the C–B–C chain quite satisfactorily but with some misfits at other axial positions. From this point of view we regard the observed disagreement as accidental but also as an example proving the necessity of collecting data sets of as high resolution as possible.

The second triangle (II), B(2)–B(2)–B(1), is bisected by a mirror plane perpendicular to the plane through the atoms (Fig. 5). Here the static deformation density distribution corroborates well the corresponding dynamic deformation density (II), but with more pronounced features. The static deformation density halfway between B(2) and B(1) is 0·20 e Å^{-3} compared to 0·12 e Å^{-3} in $d\rho_{dyn}$. The associated final residual density does not show any significant features and is therefore omitted.

In the last triangle (III), B(1)–B(1)–B(2) (Fig. 6), there is no symmetry element. The dominant finding in $d\rho_{dyn}$ was a 0·30 e Å^{-3} peak on the B(1)–B(2) bond lying in the mirror plane, which contains the asym-

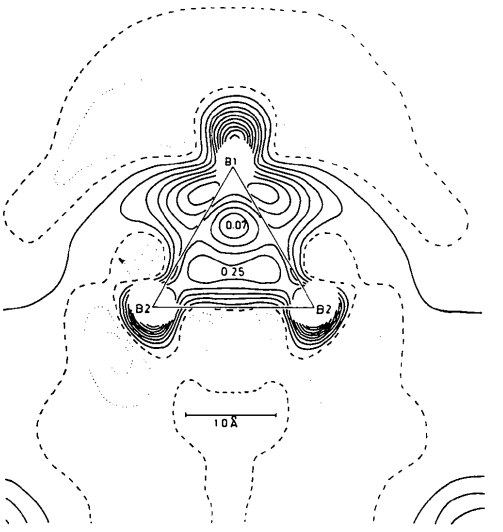

Fig. 5. Static deformation density distribution in the plane B(2)–B(2)–B(1) (triangle II). Levels at 0·05 e Å^{-3}, negative contours dotted.

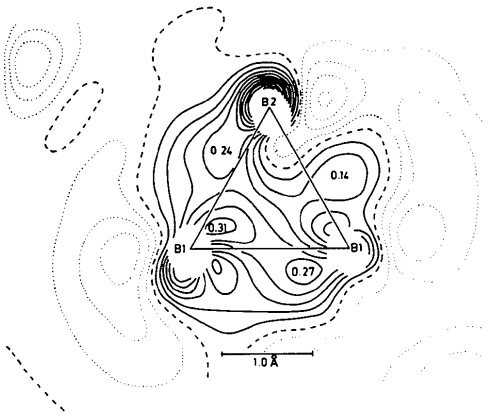

Fig. 6. Static deformation density distribution in the plane B(1)–B(1)–B(2) (triangle III). Levels at 0·05 e Å^{-3}, negative contours dotted.

metric unit (Fig. 3*a*). The pattern of the static deformation density is somewhat different. Here the other two B–B bonds are favored, whereas the maximum static deformation density on the above-quoted B(1)–B(2) bond is only 0·14 e Å^{-3}. Thus, we find another difference between the dynamic deformation density distribution expanded by the adjusted multipole functions.

Again the final residual density is insignificant and therefore omitted.

(*c*) *External bonding*

There are two types of external bonds, B(2)–B(2) connecting adjacent icosahedra and B(1)–C between the icosahedron and the C–B–C chain. Both bonds can be seen in Fig. 3(*a*). The multipoles associated with these bonds are well developed indicating strong interaction between the two structural units. For the inter-icosahedral B(2)–B(2) the final residual density (Fig. 3*c*) suggests that the static deformation density is somewhat exaggerated. In Fig. 7 all planes considered so far are depicted in one plane corresponding to unfolding the icosahedral surface and placing it on the mirror plane. Under consideration of the external bonds this view conveys that the multipole expansion at each B atom describes three differently developed lobes, which in a first approximation form a flat trigonal pyramid with one edge in the external bond direction. If we associate with each lobe one electron, the 36 valence electrons of the B_{12} icosahedron are accommodated with no need for a charge transfer from outside. Thus, the multipole expansion model emphasizes the trivalent bond character of boron, a result which is chemically reasonable and certainly contained in the real density distribution. Figs. 8 and 9 show for completeness the static deformation density distributions in the plane through the inversion center of the

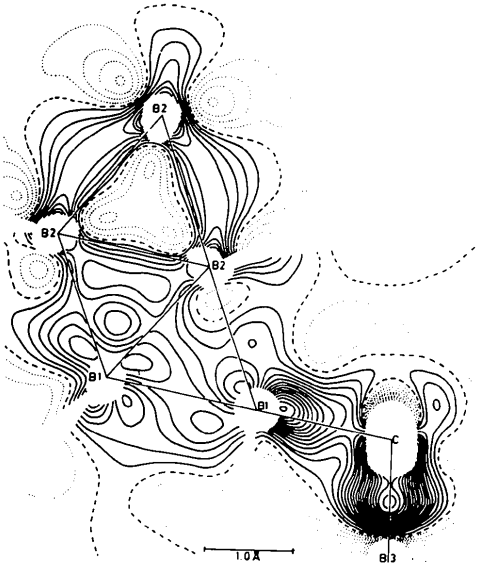

Fig. 7. Static deformation density distribution through all planes, unfolded and placed on the mirror plane. Levels at 0·05 e Å^{-3}, negative contours dotted.

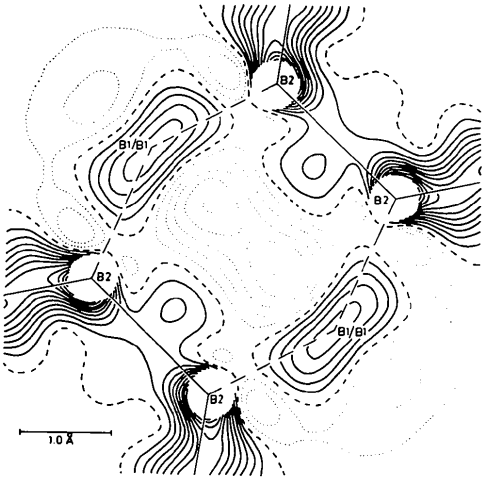

Fig. 8. Static deformation density distribution in the plane through B(2)–B(2) and the inversion center of the icosahedron. Levels at 0·05 e Å^{-3}, negative contours dotted.

icosahedron and its opposite B(2)–B(2) edges, and in the B_4C_2 ring plane. These figures are to be compared with Figs. 9 and 10(*a*) of II. Both distributions corroborate the earlier results of the dynamic deformation density investigation except the missing resolution of the charge accumulation around the B(1)/B(1) position in Fig. 8. The distribution in the B_4C_2 ring was calculated without considering the next-neighbor contributions, and the plot shows nicely the electron interaction in the hexagons forming the puckered graphite-like layers perpendicular to the *c* axis.

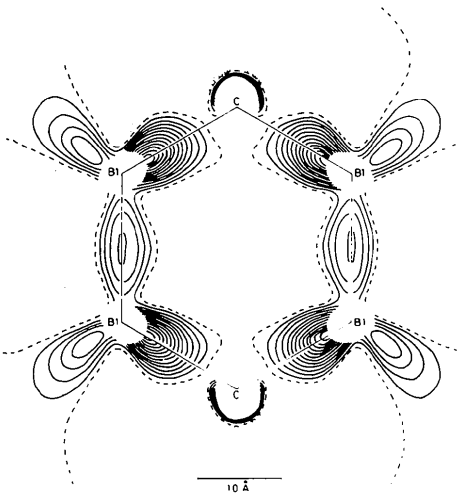

Fig. 9. Static deformation density distribution in the plane of the six-membered ring $B(1)_4C_2$. Levels at 0·05 e Å^{-3}, negative contours dotted.

Pictorial representation

For three-dimensional representations of static deformation density features we made use of the advantage that the analytical formulation of $d\rho_{stat}$ (contrary to conventional Fourier syntheses) allows the study of the refined deformation functions of individual atoms or of selected atomic arrangements by excluding undesired contributions of neighboring atoms. Resetting the multipole coefficients of such atoms to zero provides vanishing deformation densities with increasing distance from the origin in the center of the interesting object and, hence, an undisturbed view of dominant or characteristic bonding effects. The first step is to plot only one contour line at a fixed $d\rho_{stat}$ value for a number of parallel and equidistant sections of the three-dimensional space. A suitable distortion and superposition of these layers leads then to three-dimensional representations of the envelopes of the static deformation density at the desired positive or negative value (Kirfel & Will, 1980).

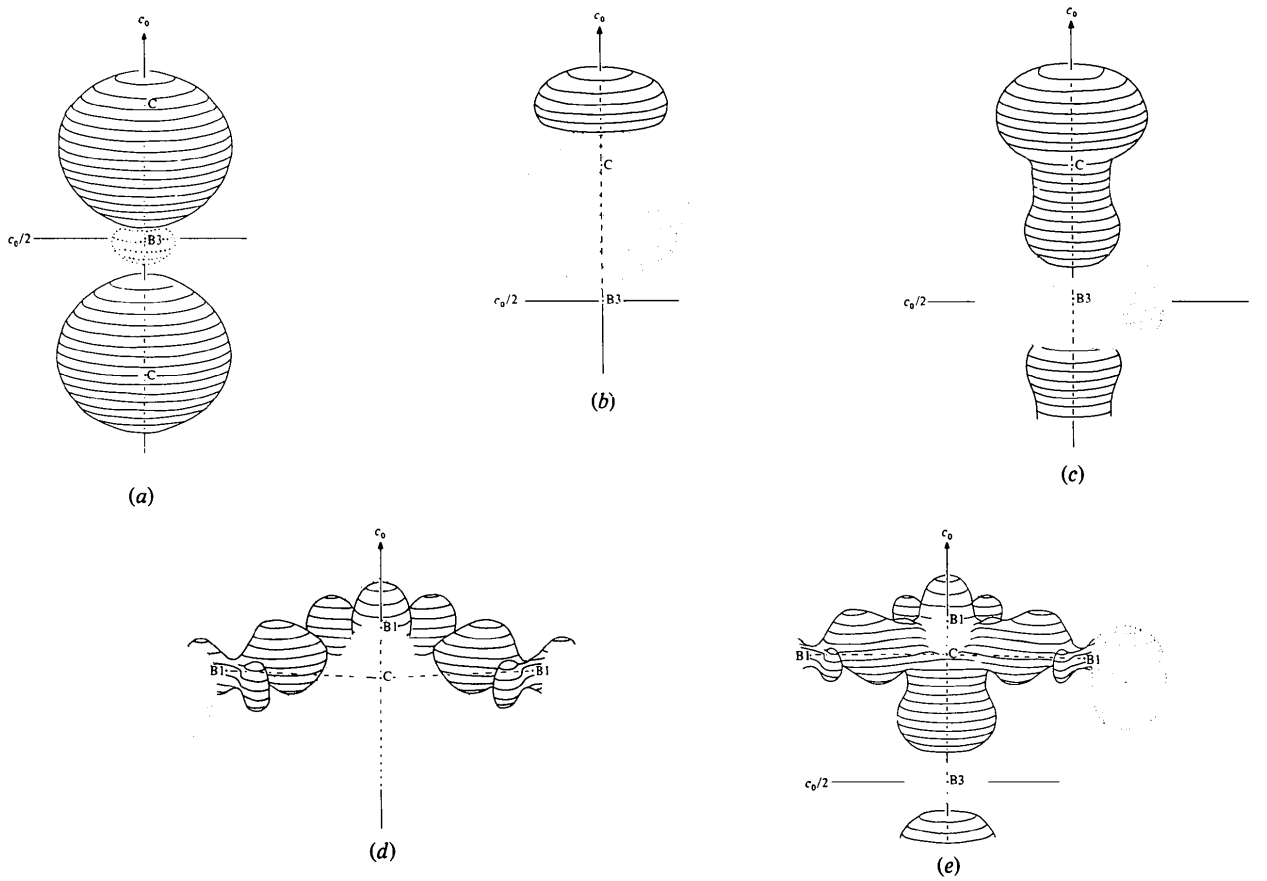

Fig. 10. Three-dimensional envelope of the positive and negative static deformation densities at $d\rho_{stat} = \pm 0{\cdot}2$ e Å^{-3}, negative contours dotted. Calculations with the multipole coefficients of (*a*) B(3); (*b*) C; (*c*) B(3) and C; (*d*) C and B(1); (*e*) B(3), C and B(1).

A series of such envelope representations calculated from the multipole functions of the chain atoms is depicted in Fig. 10(*a*)–(*e*). A critical inspection of the individual atomic deformation density distributions together with the ensuing superpositions of two or more atoms leads to the conclusion that these representations may to some extent be artefacts and therefore may convey misleading impressions. For example, the polarization of the C atom shown in Fig. 2 seems to be reversed in Fig. 10(*b*). The problem encountered with this kind of representation is the impossibility of telling from the shape of the envelope how the density changes normal to the surface. A closed envelope of a positive deformation density may still hide a trough inside, and this is the case for the C atom (see Fig. 12).

Fig. 10(*b*) shows no indication of significant contributions of the carbon deformation functions in the C–B(1) bond direction. Therefore, it seems as if only the deformation of the B(1) electron shell is responsible for the bonding between B(1) and C. Obviously, such individual atomic deformations alone do not necessarily reflect a physically meaningful picture. However, by superposition of the contributions of two or more atoms, the real picture begins to develop, and the final superposition of the multipoles of C and its surrounding B atoms, Fig. 10(*e*), clearly shows the distorted sp^3 hybrid bond character of the C atom (compare also the bond angles around C, I). Although this representation still lacks the contributions of the important neighbors next to B(1), the picture reveals the essential information on the bonding conditions at the C atom.

The reason for these findings is the redundancy of the analytical description of the model deformation density plugged into the refinement. The redundancy is also reflected in high correlation coefficients between the multipole coefficients including the α values, which describe the radial distribution of the multipoles. A subgroup of deformation functions belonging to one atom may expand an individual atomic deformation density of little significance, while at the same time the total set of deformation functions still yields an adequate description of the deviations of the electron density of the real molecule from the 'promolecule'. This point was emphasized by Hirshfeld (1971) and should be remembered in the discussion of individual atomic deformation density results, whether they are presented graphically or cast into numerical values like atomic charge or dipole moment. At present, we do not have sufficient data concerning the dependence of the multipole expansion on the application of reasonable constraints and about the best strategy of the refinement. We believe, however, that systematic investigations on the multipole expansion refinement process can improve the individual atomic expansions and thus make the presented kind of pictorial representation a useful tool for understanding and demonstrating the covalent bonding between atoms as well as the individual atomic contributions.

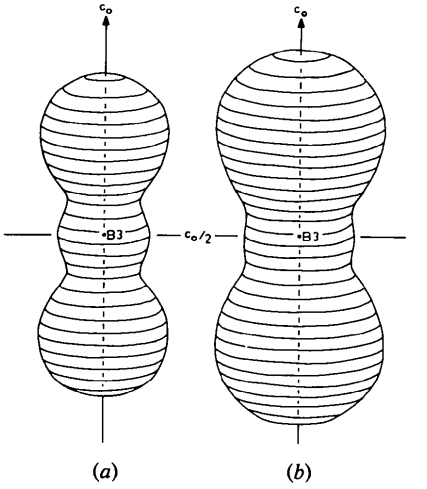

Fig. 11. Three-dimensional envelope of the total static density of B(3) at (*a*) $\rho_{stat} = 1{\cdot}0$ e Å^{-3} and (*b*) $\rho_{stat} = 0{\cdot}6$ e Å^{-3}.

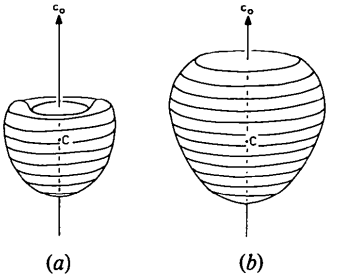

Fig. 12. Three-dimensional envelope of the total static density of the C atom at (*a*) $\rho_{stat} = 1{\cdot}0$ e Å^{-3} and (*b*) $\rho_{stat} = 0{\cdot}6$ e Å^{-3}.

The method can also be used to give pictorial representations of the *total* static electron density of one or more bonded atoms. By superposition of $d\rho_{stat}$ with the spherical free-atom electron distribution, which can be easily calculated from the Fourier transformation of the analytical scattering-factor curve (*International Tables for X-ray Crystallography*, 1974), one obtains a static total density distribution of the bonded atom(s). Under consideration of the shortcomings discussed above, such representations may still serve to give a good qualitative impression of the actual effects of chemical bonding on the electron shell. Fig. 11 shows the envelopes of the *total* static density of the central B(3) atom at $\rho_{stat} = 1{\cdot}0$ and $0{\cdot}6$ e Å^{-3}. Even under the assumption that this particular result suffers from an exaggerated expansion of the B(3) multipoles, one can easily realize how such an electron distribution can bias the vibrational parameter u_{33} in the conventional refinement (see Table 5 in I). Similar representations for the C atom are depicted in

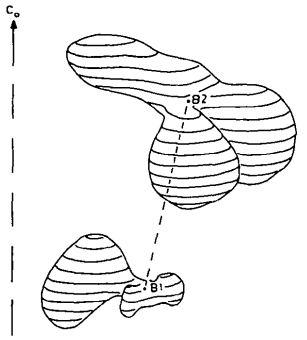

Fig. 13. Three-dimensional envelopes of the static deformation density at $d\rho_{stat} = 0{\cdot}2$ e Å^{-3}. Calculations with the multipole coefficients of B(1) and B(2).

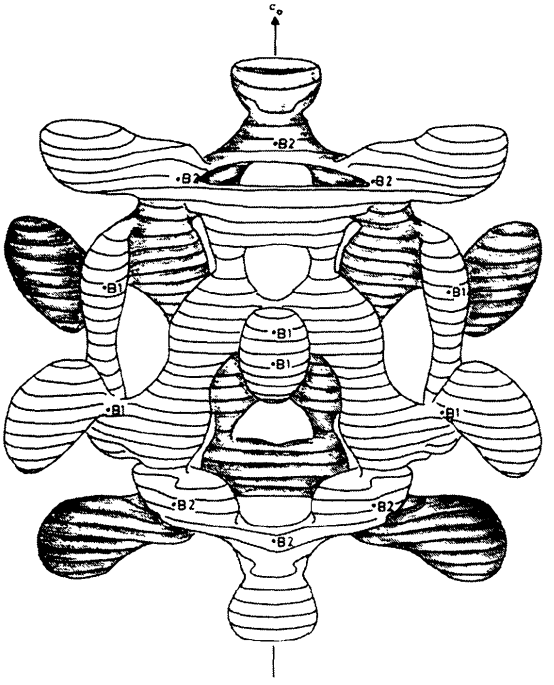

Fig. 14. Three-dimensional envelope of the static deformation density of all the atoms of the B_{12} icosahedron at $d\rho_{stat} = 0{\cdot}2$ e Å^{-3}. Calculations with the multipole coefficients of B(1) and B(2).

Fig. 12. In contrast to Fig. 10(*b*) these envelopes clearly show the significant polarization of the C atom towards B(3).

The bonding effects in the B_{12} icosahedron are much smaller than in the C—B—C chain. But we can still get a good impression of the information contained in the multipole expansion. In Fig. 13 we have depicted the envelopes of the positive static deformation densities of the two adjacent B(1) and B(2) atoms at $d\rho_{stat} = 0{\cdot}2$ e Å^{-3}. There are three lobes at each B atom, the external ones being most developed. The total icosahedral arrangement of the lobes (Fig. 14) leads to a tight network of density accumulations on the surface of the icosahedron and in the external bond directions. Both figures simply give another view of one result of the multipole expansion refinement, namely the trivalent bond character of the icosahedral B atoms.

Conclusions

The application of the multipole expansion refinement to the diffraction data ($s \leq 1{\cdot}08$ Å^{-1}) of $B_{13}C_2$ has reduced the agreement of the conventional refinement ($R = 0{\cdot}050$) by 44% to $R = 0{\cdot}028$, which corresponds to a highly significant improvement of the model. The main features of the static deformation density distribution, which is supposed to be represented by the adjusted linear combinations of localized atomic deformation functions, are in good qualitative agreement with those of the dynamic deformation density distribution. The successful description of the observed electron distribution applies especially for the linear C—B—C chain with its large bonding effects. A great deal of the model improvement is due to the proper adjustment to the chain density, which is proved by the inspection of the final residual density distribution calculated after the completion of the multipole refinement. The refinement yielded two results, which differ from the foregoing investigations. (i) There is a significant polarization of the C atom towards the central B atom in the chain. This polarization could hardly be detected from the conventional refinements (including HO) leading to bias in the vibrational parameter u_{33} of the C atom. (ii) The expansion of the icosahedral B atom multipoles emphasizes their trivalent bond character. From the comparison with the dynamic deformation density investigation, one can conclude that this result is model-biased in so far as it displays that part of the deformation of the initially spherical electron shells, which is accessible to a description by localized atomic multipoles. Since the valence electron distribution in B_{12} possesses a high degree of delocalization it is comprehensible that the applied model can deal only partially with the observed density.

The analytical form of the static deformation density distribution allows the three-dimensional pictorial representation of envelopes of the deformation density as well as of the total static density of individual atoms or molecular fragments. These representations can give useful views of bonding effects; however, the correlation problem suggests that it is better to consider fragments rather than single atoms, at least as long as individual atomic multipole expansions are not forced by external constraints to bear physical significance.

This work has received support from the Deutsche Forschungsgemeinschaft, which is gratefully acknowledged.

References

HAREL, M. & HIRSHFELD, F. L. (1975). *Acta Cryst.* B**31**, 162–172.
HIRSHFELD, F. L. (1971). *Acta Cryst.* B**27**, 769–781.
HIRSHFELD, F. L. (1976). *Acta Cryst.* A**32**, 239–244.
International Tables for X-ray Crystallography (1974). Vol. IV. Birmingham: Kynoch Press.
KIRFEL, A., GUPTA, A. & WILL, G. (1979*a*). *Acta Cryst.* B**35**, 1052–1059.
KIRFEL, A., GUPTA, A. & WILL, G. (1979*b*). *Acta Cryst.* B**35**, 2291–2300.
KIRFEL, A. & WILL, G. (1980). *Acta Cryst.* B**36**, 512–523.
LONGUET-HIGGINS, H. C. & ROBERTS, M. DE V. (1955). *Proc. R. Soc. London Ser. A*, **230**, 110–119.
REES, B. (1976). *Acta Cryst.* A**32**, 483–488.
REES, B. (1978). *Acta Cryst.* A**34**, 254–256.
WILL, G., KIRFEL, A. & GUPTA, A. (1979). *J. Less-Common Met.* **67**, 13–18.

Acta Cryst. (1980). B**36**, 1319–1322

Structure de $Tl_2Mo_9S_{11}$: Clusters Mo_{12} et Mo_6 Isolés

PAR MICHEL POTEL, ROGER CHEVREL ET MARCEL SERGENT

Laboratoire de Chimie Minérale B, Laboratoire associé au CNRS 254, *Université de Rennes, Campus de Beaulieu, avenue du Général Leclerc*, 35042 *Rennes CEDEX, France*

(*Reçu le* 12 *septembre* 1979, *accepté le* 1 *février* 1980)

Abstract

$Tl_2Mo_9S_{11}$ crystallizes in space group $R\bar{3}$, with a = 12·955 (2) Å, α = 42·09 (1)°, $Z_R = 2$ [hexagonal axes: a = 9·304 (3), c = 35·366 (7) Å], d_m = 5·27, d_x = 5·34 Mg m^{-3}. The structure has been determined by direct methods and refined by least squares to R = 0·032, R_w = 0·033 for 1410 independent reflections. The structure consists of a stacking of Mo_6S_8–Tl–Tl–$Mo_{12}S_{14}$ files which run along the ternary axis; these lead to normal octahedral Mo_6 clusters and new trioctahedral Mo_{12} clusters which can be described as a linear condensation of three Mo_6 clusters.

Introduction

Dans des publications précédentes, nous avons montré que les chalcogénures dérivant du Mo^{II} se caractérisent par la présence, dans leur structure, de clusters octaédriques Mo_6. Récemment, nous avons préparé une nouvelle phase dérivant du Mo^{II} possédant des clusters Mo_6 et Mo_9 dans des motifs Mo_6Se_8 et Mo_9Se_{11} (Chevrel, Sergent, Seeber, Fischer, Grüttner & Yvon, 1979; Grüttner, Yvon, Chevrel, Potel, Sergent & Seeber, 1979; Seeber, Decroux, Fischer, Chevrel, Sergent & Grüttner, 1979). Nous décrivons ici la structure d'une nouvelle phase à cluster plus condensé, $Tl_2Mo_9S_{11}$, qui possède à la fois des clusters Mo_6 et Mo_{12} dans des motifs Mo_6S_8 et $Mo_{12}S_{14}$ respectivement.

0567-7408/80/061319-04$01.00

Partie expérimentale

Le composé $Tl_2Mo_9S_{11}$ est obtenu par synthèse directe à partir des éléments (Chevrel, Potel, Sergent, Decroux & Fischer, 1980). Les mélanges 2Tl + 9Mo + 11S sont effectués en boîte à argon désoxygéné et, dans un premier temps, portés à 1123 K, dans un tube de silice scellé sous vide. Un recuit vers 1373 K est nécessaire pour obtenir un produit pur. Des monocristaux noirs, stables à l'air, généralement de forme rhomboédrique allongée, sont obtenus par chauffage prolongé à 1423 K.

L'étude radiocristallographique préliminaire a été menée sur chambre photographique de Weissenberg et de précession. Les paramètres de la maille cristalline

Tableau 1. *Conditions de l'enregistrement et de l'affinement*

Dimensions du cristal utilisé	0,07 × 0,1 × 0,1 mm
Coefficient linéaire d'absorption	μ = 18,33 mm^{-1} ($\bar{\mu}R \simeq 1$)
Radiation utilisée	Mo $K\bar{\alpha}$ (λ = 0,71069 Å)
Monochromateur	Lame de graphite
Distance cristal–détecteur	173 mm
Limite d'enregistrement	$\theta \leq 30°$
Balayage	ω–2θ
Amplitude de balayage	(1 + 0,35 tg θ)°
Ouverture	(2 + 0,35 tg θ)mm
Nombre de réflexions non nulles enregistrées	3078
Nombre de réflexions indépendantes	1410
Valeur finale du R	0,032
Valeur finale du R_w	0,033